Chemical Senses, 2019, Vol 44, 173–188
doi:10.1093/chemse/bjz005
Original Article
Advance Access publication 18 January 2019

Original Article

A Novel Olfactometer for Efficient and Flexible Odorant Delivery

Shawn D. Burton[1], Mia Wipfel[2,*], Michael Guo[2,*], Thomas P. Eiting[1] and Matt Wachowiak[1]

[1]Department of Neurobiology and Anatomy, University of Utah, Salt Lake City, UT 84112, USA and [2]Department of Biomedical Engineering, University of Utah, Salt Lake City, UT 84112, USA

Correspondence to be sent to: Matt Wachowiak, Department of Neurobiology and Anatomy, University of Utah, Salt Lake City, UT 84112, USA. e-mail: matt.wachowiak@utah.edu

*These authors contributed equally to the work.

Editorial Decision 11 January 2019.

Abstract

Understanding how sensory space maps to neural activity in the olfactory system requires efficiently and flexibly delivering numerous odorants within single experimental preparations. Such delivery is difficult with current olfactometer designs, which typically include limited numbers of stimulus channels and are subject to intertrial and interchannel contamination of odorants. Here, we present a novel olfactometer design that is easily constructed, modular, and capable of delivering an unlimited number of odorants in air with temporal precision and no detectable intertrial or interchannel contamination. The olfactometer further allows for the flexible generation of odorant mixtures and flexible timing of odorant sequences. Odorant delivery from the olfactometer is turbulent but reliable from trial to trial, supporting operant conditioning of mice in an odorant discrimination task and permitting odorants and concentrations to be mapped to neural activity with a level of precision equivalent to that obtained with a flow dilution olfactometer. This novel design thus provides several unique advantages for interrogating olfactory perception and for mapping sensory space to neural activity in the olfactory system.

Key words: calcium imaging, olfaction, olfactory bulb, operant conditioning, plume

Introduction

Mapping sensory information to neural activity in the olfactory system is complicated by many factors, including the high dimensionality of olfactory stimulus space and limited knowledge of odorant receptor tuning. Overcoming these difficulties often requires testing large numbers of odorants to adequately cover even a portion of olfactory stimulus space, creating a need for methods of odorant delivery that are both efficient (i.e., tens to hundreds of odorants testable per preparation) and flexible (i.e., odorants chosen "on the fly" during the course of an experiment).

Efficient and flexible odorant delivery can be achieved by manually presenting odorant reservoirs to the experimental preparation (e.g., see Takahashi et al., 2004). However, such manual presentation involves long, variable, and relatively uncontrolled odorant delivery. Flow dilution olfactometers, which are widely used throughout olfactory research, instead enable automated delivery of temporally controlled streams of precisely diluted odorants using a combination of tubing, computer-controlled valves, and mass flow controllers (Bodyak and Slotnick, 1999; Slotnick and Restrepo, 2005; Johnson and Sobel, 2007; Schmidt and Cain, 2010). Flow dilution olfactometers have substantial limitations, however. For example, intertrial and interchannel contamination can arise from adsorption of odorants to surfaces downstream of odorant reservoirs (e.g., tubing, manifolds, mixing chambers, and final delivery ports), as well as from pressure fluctuations during valve actuation that can generate backflow of odorant vapor into upstream manifolds. Consequently, delivering numerous odorants with flow dilution olfactometers requires frequent and careful washing and/or replacement of multiple components, substantially reducing delivery efficiency and flexibility. Less standard flow dilution olfactometers using large multichannel odorant banks (e.g., see Davison and Katz, 2007; Soucy et al., 2009; Tan et al., 2010) can achieve efficient odorant delivery but are still subject to intertrial and interchannel contamination, provide limited delivery flexibility, and can be expensive to build.

Here, we describe and characterize an olfactometer capable of efficient and flexible odorant delivery with minimal interchannel and intertrial contamination. The novel design incorporates interchangeable modules with inexpensive and disposable odorant reservoirs that can be prepared during the course of an experiment and uses spans of open airflow instead of tubing to eliminate common adsorptive surfaces that can give rise to contamination. Through these design features, the olfactometer generates turbulent yet temporally precise odorant delivery at adjustable concentrations and further allows for flexible generation of vapor-phase odorant mixtures as well as "rapid-fire" sequences of odorants. Using this olfactometer to monitor sensory-evoked neural activity in the mouse olfactory system, we routinely test >100 odorants chosen on the fly in a single experimental preparation, with multiple trials per odorant, and observe reliable odorant-evoked activity patterns with no detectable intertrial or interchannel contamination. We further demonstrate that the olfactometer readily supports behavioral testing in an operant conditioning odorant discrimination task. The novel olfactometer design thus provides several key advantages for probing olfactory perception and for mapping high-dimensional olfactory stimulus space to neural activity.

Materials and methods

Olfactometry

Odorants were acquired from Sigma-Aldrich, except for isoamyl acetate, which was acquired from MP Biomedicals, and methyl tiglate, which was acquired from Tokyo Chemical Industry Co., Ltd. Odorants were diluted in caprylic/capric medium chain triglycerides (C3465, Spectrum Chemical Mfg. Corp.). Characterization of olfactometer performance was completed using a photoionization detector (PID) (200B miniPID, Aurora Scientific), with the following olfactometer operating parameters held constant (unless otherwise stated): olfactometer-to-PID distance: 8–10 cm; channel pressure: 30 kPa; carrier stream flow rate: 8 L/min; odorant: (+)-α-pinene (1:5–10 liquid dilution). When evaluating the influence of each operating parameter on odorant delivery from the olfactometer, the parameter was systematically varied across interleaved trials (e.g., trial 1: 5 kPa channel pressure; trial 2: 10 kPa channel pressure; trial 3: 15 kPa channel pressure) using a single odorant reservoir to minimize any variability due to odorant depletion or slight differences in odorant reservoir preparation. Carrier stream airspeeds were measured using a Solomat 510e Multi-Function Indoor Air Quality and Environmental Monitor with hot-wire anemometer. To estimate the concentration of odorant delivery as a fraction of saturated odorant vapor, odorant delivery from the novel olfactometer and a previously described flow dilution olfactometer (Verhagen et al., 2007) were compared.

Animals

For neural imaging experiments, olfactory marker protein (OMP)-Cre mice (Li et al., 2004) were crossed to Rosa26-CAG-lox-STOP-lox-GCaMP6f (RCL-GCaMP6f) mice (Madisen et al., 2015). Female offspring heterozygous (Figure 10) or homozygous (Figure 11) for the OMP-Cre allele and 2–4 months in age were used. Mice were housed 5 per cage with food and water available ad libitum. For behavioral experiments, 3 C57BL/6 mice (1 male, 2 female) 2–6 months in age were used. All mice were kept on a 12-h-light/dark cycle. All procedures were performed following the National Institutes of Health *Guide for the Care and Use of Laboratory Animals* and were approved by the University of Utah Institutional Animal Care and Use Committee.

Neural imaging

Imaging was performed essentially as described previously (Wachowiak and Cohen, 2001). Briefly, mice were initially anesthetized with intraperitoneal injection of pentobarbital (50 mg/kg) and subcutaneous injection of chlorprothixene (12.5 mg/kg). Subcutaneous injection of atropine (0.5 mg/kg) was additionally provided to minimize mucus secretions and maintain nasal patency. Heart rate and body temperature were maintained at 300–500 beats per minute and 37 °C, respectively, throughout the experiment. A double tracheotomy was performed and inhalation artificially controlled (rates: 1–3 Hz) via the ascending tracheal tube (Eiting and Wachowiak, 2018). For imaging, mice were head-fixed and the bone over the dorsal main olfactory bulbs thinned. Anesthesia was maintained by ~0.5% isoflurane delivered in pure O_2 to the descending tracheal tube. Widefield epifluorescence signals were acquired with a 4×, 0.28 NA or 5×, 0.25 NA objective (Olympus) at 256 × 256-pixel resolution and 25-Hz-frame rate using a back-illuminated charge-coupled device camera (NeuroCCD-SM256; RedShirt Imaging) and Neuroplex software, with illumination provided by a 470 nm LED (M470L2, Thorlabs) and green fluorescent protein filter set (GFP-1828A-000, Semrock).

Behavior

Behavioral testing was modified from previously published protocols (Verhagen et al., 2007; Wachowiak et al., 2013). Briefly, mice were anesthetized with isoflurane, and a custom aluminum headbar was glued and then cemented (Teets Denture Material, Cooralite Dental Mfg. Co.) to the skull. Mice were given carprofen (5 mg/kg) and enrofloxacin (5–10 mg/kg) for 2 days post-surgery and housed individually with food and water available ad libitum. Approximately 1 week after headbar implantation, mice were water restricted to provide motivation for behavioral testing. Specifically, mice were limited to 1.0 mL of water per day, until their body weight fell to 80–85% of their pre-restriction weight. Once criterion weight was reached, mice were habituated for 2–3 days to the experimenter, the behavioral testing apparatus, and the behavioral tasks. The apparatus consisted of an air-floated Styrofoam ball and bar capable of fastening to the implanted headbar, enabling head-fixation of the mouse while otherwise permitting free movement. A lickspout dispensing fresh water was placed ~5 mm from the mouth of the mouse, with water delivery in ~12 μL increments triggered by a solenoid valve on correct task response. The task consisted of a standard go/no-go olfactory discrimination task, with 4-s-long odorant presentations. Mice were trained to lick for water reward during the presentation of a conditioned stimulus (CS+) odorant and to withhold licking during an unconditioned stimulus (CS–) odorant.

Data analysis

Odorant delivery latencies were calculated as the delay from valve actuation to the first deviation of the PID signal ≥3 × standard deviations (SDs) from the baseline. Odorant delivery durations were calculated as the difference between the first and last deviations of the PID signal ≥3 × SD from the baseline. In neural imaging experiments, glomeruli were identified by manually drawing regions of interest (ROIs) around glomerular-sized foci of activity. ΔF/F responses were calculated by first subtracting the mean signal over the 1 s preceding odorant delivery onset (i.e., the resting fluorescence) from the mean signal over the 2–3 s following odorant delivery onset, and then dividing by the resting fluorescence. ROI ΔF/F timecourses and correlation values were then derived using the mean ΔF/F across all pixels within an ROI. For display, odorant response maps were filtered with a Gaussian kernel (σ = 0.75 pixels), upsampled with bilinear interpolation to 512 × 512-pixel resolution, and pseudocolored for clarity. All shaded regions and error bars depict mean ± SD.

Results

To enable efficient and flexible delivery of odorants with controllable timing, adjustable concentration, and minimal intertrial and interchannel contamination, we designed a novel modular olfactometer that uses spans of open airflow instead of tubing to both minimize adsorptive surfaces and facilitate rapid exchange of inexpensive disposable odorant reservoirs.

Construction and operation

Similar to the general operating principle of flow dilution olfactometers, the novel olfactometer uses computer-controlled valves to direct air into an odorant reservoir, which expels saturated odorant vapor into a diluting carrier stream that is then directed to the experimental preparation. Distinct from flow dilution olfactometers, however, the novel olfactometer integrates spans of open airflow both immediately upstream and downstream of the odorant reservoirs (Figure 1A). The complete open flow of air downstream of the odorant reservoirs (Figure 1B–E) dramatically reduces the available surfaces to which expelled odorants can adsorb, thus minimizing intertrial contamination of one odorant with another. Moreover, the spans of open airflow upstream of the odorant reservoirs eliminate the possibility of odorant backflow into upstream components, minimizing the potential for interchannel contamination. Another critical feature of the novel design is the use of small disposable odorant reservoirs attached in sets of 12 to modular barrels. This feature enables numerous 12-odorant panels to be flexibly loaded and rapidly exchanged during an experiment.

The novel olfactometer includes 2 main components: 1) a delivery arm, which directs odorant delivery to the experimental preparation; and 2) a flow control housing, containing airflow controls (Figure 1A; Table 1).

The delivery arm comprises a single base and multiple modular barrels (Figure 2). The base is constructed around a machined annular cylinder (outer diameter: 8.60 cm [~3 $^{3}/_{8}$ in]; inner diameter: 1.91 cm [~$^{3}/_{4}$ in]; height: 1.27 cm [~$^{1}/_{2}$ in]) through which the carrier stream tube fits snugly. The carrier stream tube is further secured with a set screw (#10–32 thread) tapped into the base cylinder (data not shown). In the design illustrated, we have used 2 concentric carrier stream tubes to broaden the final carrier stream of air at the delivery arm output, but in practice a single carrier stream tube suffices. An additional hole (#1/4–20 thread) tapped into the base cylinder is used to connect to an articulating dial gauge holder (Figure

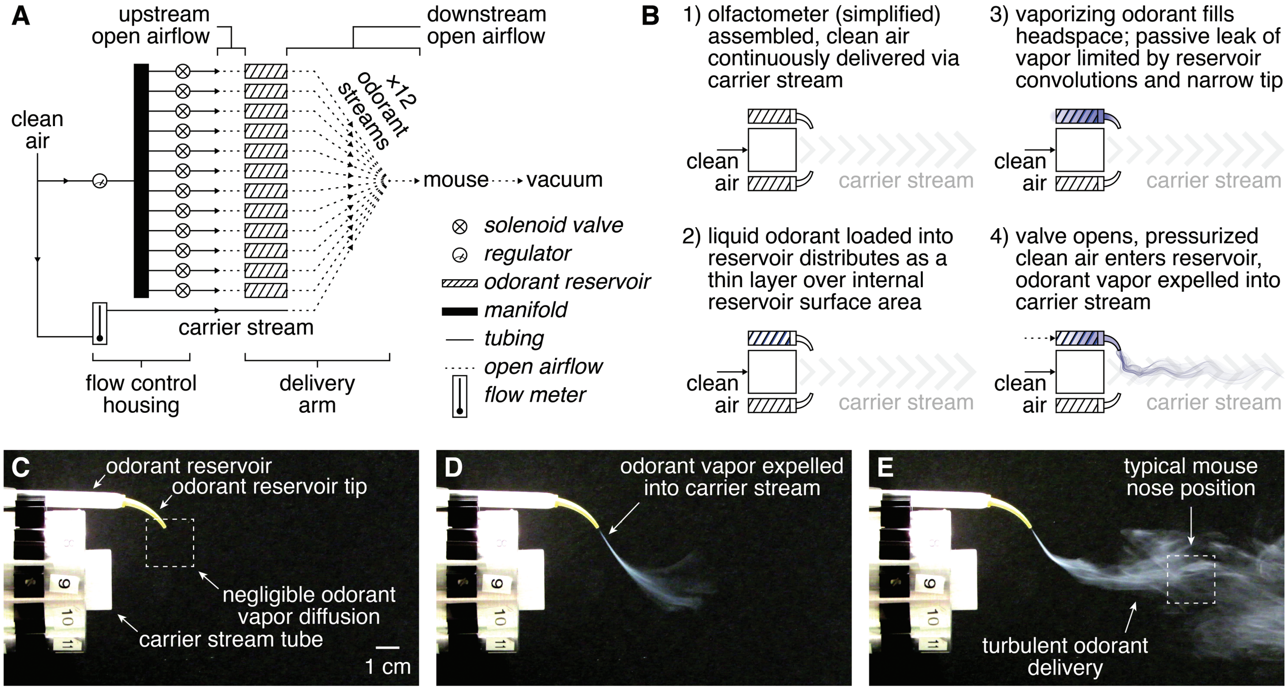

Figure 1 Operation of the novel olfactometer. (**A**) Pressurized clean air is directed through a manifold to 12 independent normally closed solenoid valves. Following valve actuation, pressurized air flows across a short unconfined region (i.e., a span of open airflow) before entering a disposable odorant reservoir, expelling saturated odorant vapor from the reservoir into the central carrier stream. Bulk flow carries the final odorized stream across a span of open airflow (typically 8–10 cm) to the experimental preparation (e.g., a mouse for neural imaging and/or behavioral testing). Odorized air not sampled by the preparation is continuously scavenged through an exhaust vacuum situated behind the experimental preparation. (**B**) Simplified illustration of operation, with 2 odorant reservoirs depicted for visual clarity. (**C–E**) Images of vaporized $TiCl_4$ delivery from the olfactometer (delivery arm only shown) immediately before valve actuation (**C**), immediately following valve actuation (**D**), and following mixing of the expelled $TiCl_4$ with the carrier stream (**E**). Only a single odorant reservoir (of 12 possible) was used for visual clarity.

Table 1 Olfactometer parts list

Olfactometer component	Part	Supplier (cat. #)	Qty. per olfactometer
Flow control housing[a]	Solenoid valve	Clippard (EW-2M-24-L)	12
	Valve manifold	Clippard (15482-12)	1
	Barbed connector	Clippard (CT2)	12
	Solenoid valve driver	Mouser Electronics (998-MIC2981/82YN)	2
	Terminal board	Winford Engineering (DTA3520-DIN)	2
	DAQ device	National Instruments (782604-01)	1
	24 V power supply	Jameco Electronics (1940547)	1
	Flow meter	Aalborg (PMR1-012676)	1
	Pressure regulator	Clippard (MAR-1–2)	1
	Pressure sensor display	Keyence (AP-34KP)	1
Connections	Polyurethane Tubing	Clippard (URH8-0402-02T-050; URH1-0804)	1
Delivery arm base	Base	custom-machined, aluminum[b]	1
	Base magnets	K&J Magnetics, Inc. (D42)	3
	Barbed connector	Clippard (CT2)	24
	Carrier stream tube	McMaster-Carr (45375K734), custom-machined[b]	1
	Carrier stream tube set screw	McMaster-Carr (92311A431)	1
	Carrier stream tube connector	Cole-Parmer (EW-06381-82)	1
	Articulating dial gage holder	Noga (e.g., MA61003)	1
	Eductor (optional)	United States Plastic Corp. (62472)	1
Delivery arm barrel (multiple [×] recommended)	Barrel	Custom-machined, aluminum[b]	×
	Barrel magnets	K&J Magnetics, Inc. (D42)	3×
	Odorant reservoir fastener	Digi-Key Electronics (RPC1280-ND)	12×
	Fastener screws	McMaster-Carr (91099A104)	12×
Disposables (1 per odorant tested)	Odorant reservoir	McMaster-Carr (74695A951)	—
	Odorant reservoir tip	Henry Schein (3124396)	—

[a] Suggested wiring diagram and example National Instruments LabVIEW code available on request.

[b] Computer-aided design files available on request.

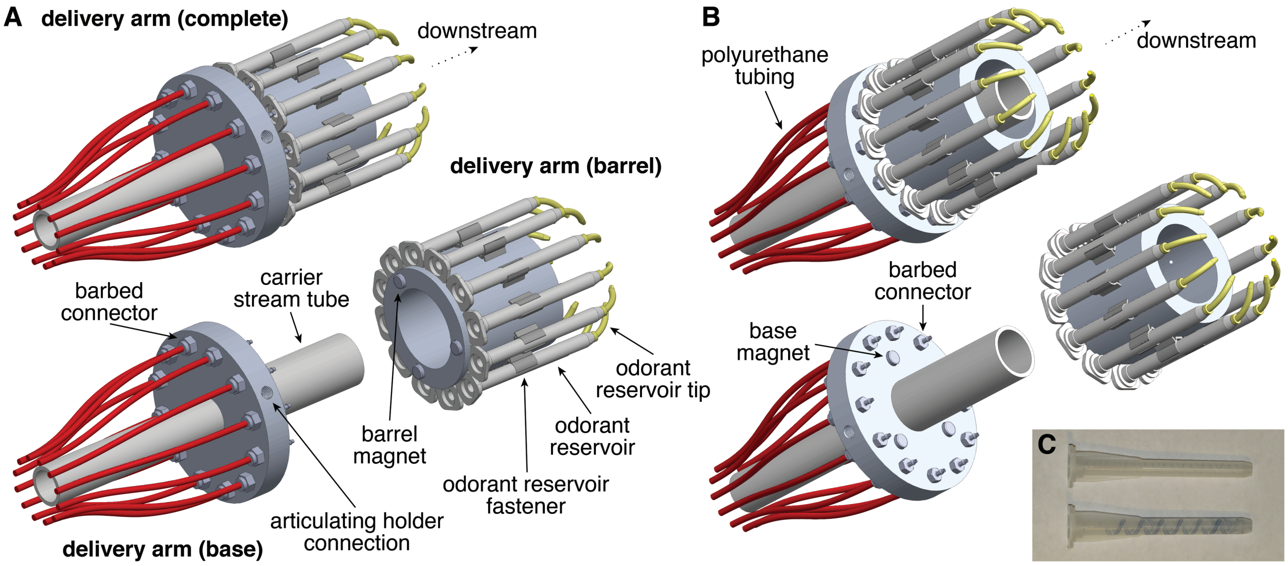

Figure 2 Construction of the novel olfactometer delivery arm. (**A** and **B**) Rotated view of the upstream (**A**) and downstream (**B**) surfaces of the olfactometer delivery arm, demonstrating magnetic attachment of modular barrels containing odorant reservoirs. (**C**) Image of 2 odorant reservoirs before (upper) and after (lower) being loaded with odorant dissolved in caprylic/capric medium chain triglycerides containing trace quantities of Sudan Black B. Gravity and surface tension drive the liquid odorant to distribute in a thin layer over the helical projections within the reservoir.

2A), allowing the delivery arm to be easily and stably positioned on any conventional air table. Twelve channels (#10–32 thread) are tapped through the base cylinder, and barbed connectors attached at both ends of each channel; connectors on the upstream surface (Figure 2A) connect to polyurethane tubing (Figure 2B) leading to independent solenoid valves within the flow control housing, whereas connectors on the downstream surface (Figure 2B) direct airflow toward the bottom of each odorant reservoir when the barrel is assembled with the base. Importantly, these latter connectors do not physically touch the odorant reservoirs, creating a span of open airflow upstream of each reservoir (Figure 1A) that minimizes contamination and facilitates rapid exchange of preloaded barrels without requiring any components to be physically disconnected. To further accelerate this exchange and to ensure proper alignment of the base and barrel, 3 magnets are adhered in an asymmetric pattern to the downstream surface of the base cylinder (Figure 2B) and three more to the upstream surface of each barrel (Figure 2A).

The barrel is constructed around a machined annular cylinder (outer diameter: 6.00 cm [~2 $^3/_8$ in]; inner diameter: 4.00 cm [~1 $^1/_2$ in]; height: 6.00 cm [~2 $^3/_8$ in]) that easily passes over the carrier stream tube (Figure 2A and B). Twelve holes (#2–56 thread) are tapped into the barrel cylinder (data not shown) and used to attach the odorant reservoir fasteners (Figure 2A). Odorant reservoirs are repurposed mixers for 2-part adhesives that are mass produced for a variety of applications and so are relatively inexpensive and readily available in large quantities. Helical projections comprising the internal structure of each mixer provide extensive surface area over which liquid odorant distributes in a thin layer (Figure 2C), yielding a disposable reservoir with small headspace that rapidly saturates with odorant vapor (Figure 1B). After loading, reservoirs easily snap into the fasteners with slight pressure and are then capped with tightly fitting disposable tips (Figure 2A) repurposed from dental applicators that, similar to the odorant reservoirs, are also relatively inexpensive and readily available in large quantities. Odorant reservoir tips serve 2 functions: 1) the narrow tip aperture, together with the internal convolutions of the odorant reservoirs, effectively limits diffusion of odorant vapor out of loaded reservoirs while still permitting pressurized air puffs to expel odorant vapor (Figure 1B; cf. Figure 1C and D); and 2) following valve actuation, the curved tip geometry directs expelled odorant vapor from the reservoir into the carrier stream (Figure 1B,D and E).

The parameters of odorant delivery, including which of the odorants loaded into the modular barrel, are delivered to the experimental preparation, as well as the specific time and concentration of odorant delivery, are governed by components within the flow control housing (Figure 1A). Clean air enters the flow control housing and is passed to the upstream end of the delivery arm carrier stream tube through a polyurethane tube at a constant rate controlled by a simple manual flow meter. In parallel, clean air from a separate source (or split from the same source as described earlier) is split by a manifold into 12 separate channels, each of which connects to the inlet of an independently controlled, normally closed solenoid valve. A single miniature manual regulator upstream of the manifold controls the pressure of clean air at all 12 valves, such that changes in pressure uniformly influence delivery across all 12 channels. Polyurethane tubing connects valve outlets to the corresponding barbed connectors on the upstream surface of the delivery arm base. Odorant delivery is achieved and temporally controlled by actuation of a valve to the open state, which releases pressurized clean air into the upstream end of an odorant reservoir, expelling saturated odorant vapor out of the odorant reservoir tip and into the continuously flowing carrier stream ~5–10 cm from the downstream end of the carrier stream tube (Figure 1B–E). As visualized with vaporized $TiCl_4$, odorant is thus delivered in a relatively broad stream by bulk flow via the carrier stream (Figure 1E); a downstream exhaust vacuum (Figure 1A) is thus highly recommended to both further direct the flow of odorant vapor to the experimental preparation and to scavenge excess odorant after it has passed by the preparation. Clearance of excess odorant is further promoted by the continuous delivery of clean air via the carrier stream when all 12 valves are closed, which additionally minimizes potential nonspecific odorant input to the experimental preparation arising from the laboratory environment or the experimental preparation itself.

In our implementation, valve actuation is controlled by a National Instruments data acquisition (DAQ) USB device and custom National Instruments LabVIEW code (Table 1), though we note that other, more economical alternatives (e.g., Arduino) could easily be used. Actuation of each valve is independently controlled by digital outputs from the DAQ device routed through terminal board-mounted high-voltage driver arrays. Other components of the DAQ device are used for additional control options, such as 1) external triggering of valve actuation, 2) an analog input channel for recording PID signals, and 3) an analog output channel encoding odorant identity.

At current prices, construction of the novel olfactometer (excluding the few custom-machined components) totals ~$1500.00, with each odorant tested costing an additional ~$1.00 in disposables (i.e., odorant reservoir and odorant reservoir tip).

Characterization of odorant delivery

Visualization of odorant delivery from the novel olfactometer using vaporized $TiCl_4$ revealed turbulent plumes (Figure 1E). Effective implementation of the olfactometer will thus require careful consideration and understanding of this variable stimulus profile and its dependence on various operating parameters. Therefore, we next systematically characterized the performance of the olfactometer using a PID across a range of operating parameters.

We first examined the profile and consistency of odorant delivery from the 12 olfactometer channels. On single trials, 2-s-long valve openings drove turbulent delivery of odorant (Figure 3A) with PID signals spanning frequencies of ~0–20 Hz (Figure 3C). While turbulent, the overall envelope of odorant delivery was reliable from trial to trial, such that averaging PID signals across multiple trials yielded steplike profiles (Figure 3B) comparable with the profile of odorant delivery from a flow dilution olfactometer. Delivery was similar across each of the 12 channels, with comparable odorant delivery mean (i.e., concentration) and variance (Figure 3D and E). Likewise, the latency from valve opening to odorant delivery was consistent across the 12 channels (Figure 3F), though longer than observed with flow dilution olfactometers, which are typically positioned much closer to the experimental preparation (i.e., 0–2 cm vs. 5–10 cm). Repositioning the PID to upstream of the odorant reservoir revealed no or negligible odorant backflow (data not shown), and in practice any such backflow would be scavenged by typical exhaust systems positioned around the experimental setup. In total, the olfactometer thus mediates turbulent but overall reliable and comparable odorant delivery across 12 independent channels.

Saturated odorant vapor expelled from the odorant reservoir visibly disperses within the carrier stream as distance from the olfactometer increases (Figure 1E). Systematically varying the distance between the PID and the downstream end of the carrier stream tube quantitatively confirmed this observation (Figure 4A and B). The highest mean concentration of odorant was detected where the expelled saturated odorant vapor first entered the carrier stream (~6 cm), with monotonic decreases in delivery mean (Figure 4C) and variance (Figure 4D) and a monotonic increase in latency as distance increased (Figure 4E). At the longest distances tested, the profile of odorant delivery further exhibited fewer high-frequency components (Figure 4F). Even with the distance-dependent decline in mean concentration, however, reliable odorant delivery with predictable latencies was still achieved with olfactometer-to-PID distances up to ~12 cm. The olfactometer can thus easily accommodate a variety of experimental paradigms (e.g., the concurrent positioning of a lick-spout for operant conditioning).

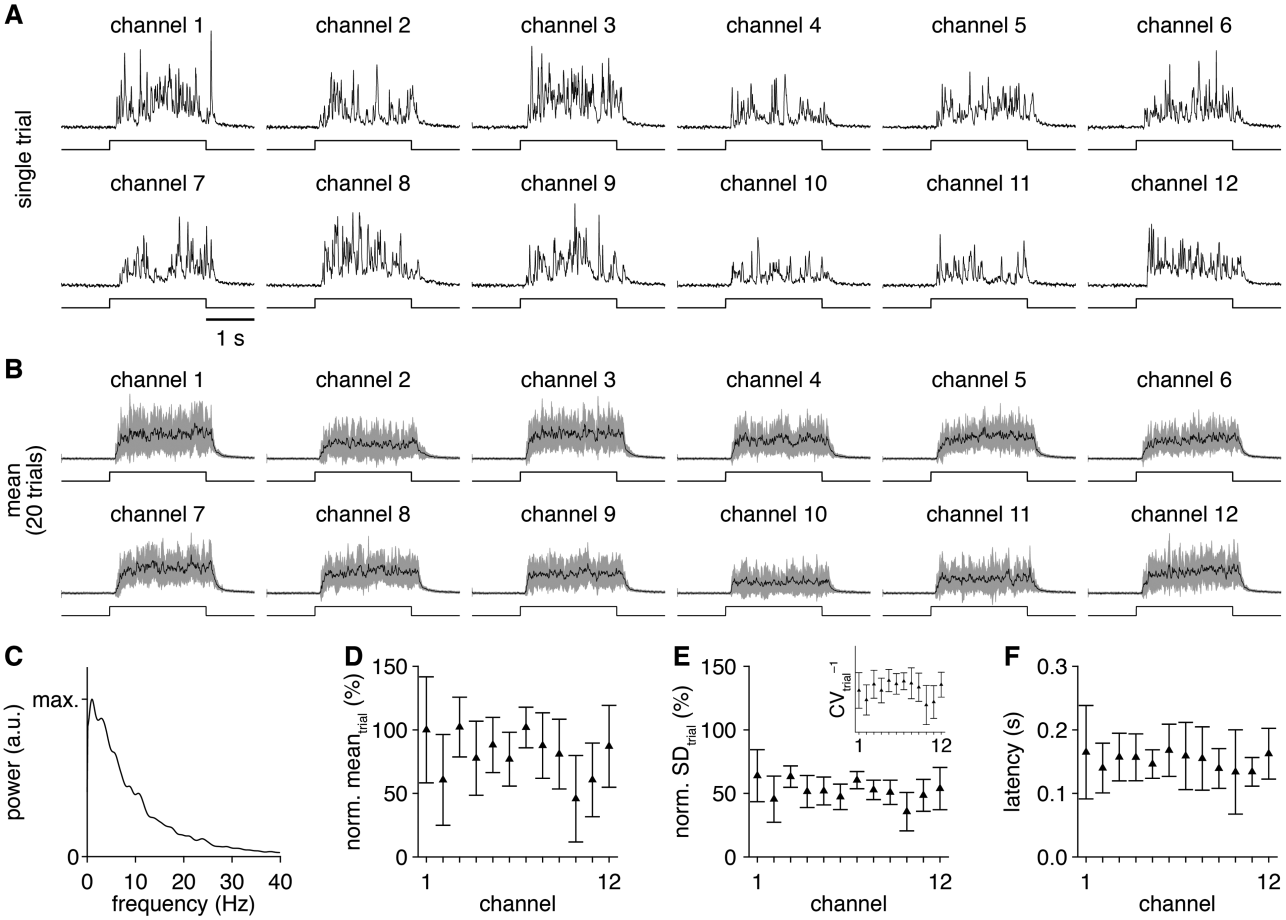

Figure 3 Comparable odorant delivery across 12 distinct channels. (**A**) PID recordings (upper) during single trials of 2-s-long valve openings (lower) from each olfactometer channel. (**B**) Mean PID recording across 20 trials for each olfactometer channel. (**C**) Mean power spectrum, averaged across all channels and trials. (**D** and **E**) PID recording mean (**D**) and SD (**E**) during the odorant delivery for each channel (normalized to the channel 1 mean). Inset: inverse of the coefficient of variation for each channel, reflecting the strength of odorant delivery relative to the delivery variability. (**F**) Mean latency of odorant delivery for each channel.

On first principles, increasing the pressure of clean air at the channel valve should increase the rate of airflow through the odorant reservoir following valve actuation, thus increasing the amount of saturated odorant vapor expelled into the carrier stream. Indeed, we observed a monotonic increase in the mean concentration (and variance) of odorant delivery (Figure 5A,B,D and E) with increasing channel pressure. In contrast, there was no detectable change in the ratio of high-to-low frequency components in the odorant delivery profile (data not shown), and the latency of odorant delivery was minimally affected at channel pressures ≥10 kPa and essentially identical for channel pressures 20–40 kPa (Figure 5F). Varying channel pressure thus provides a convenient avenue for instantaneously modulating the mean concentration of odorant delivery. To estimate the range of concentrations achievable through channel pressure modulation in an intuitive format, we directly compared delivery of the same odorant from the novel olfactometer versus a flow dilution olfactometer (Figure 5C; see Materials and methods). Relating the PID signals obtained with varying channel pressures versus varying air dilutions of saturated vapor, we found that channel pressure can modulate the mean concentration of odorant delivery over a range equivalent to ~0.5–2.5% saturated odorant vapor (Figure 5G), depending on other operational parameters (e.g., decreasing the olfactometer-to-experimental preparation distance will shift this range to higher values).

In contrast to changes in channel pressure, varying the carrier stream flow rate strongly modulated the temporal properties of odorant delivery. Lower flow rates yielded both longer and more variable odorant delivery latencies (Figure 6A–C), as well as fewer high frequency components in the profile of odorant delivery (Figure 6A and D), consistent with previous results using a fan to generate turbulent odorant plumes (Nagel and Wilson, 2011). Surprisingly, with the exception of flow rates ≤2 L/min (which resulted in unreliable odorant delivery), this modulation of temporal properties occurred with minimal changes in the mean concentration of odorant delivery (Figure 6B and E), suggesting that the expelled saturated odorant vapor is incompletely mixed in the carrier stream. Modulating the carrier stream flow rate thus provides a simple method for investigating how varying plume dynamics impact neural activity and olfactory perception.

Different experimental paradigms require variable stimulus durations. Therefore, we next examined the resolution of odorant delivery duration afforded by the novel olfactometer. Valve opening durations as short as 20 ms yielded detectable odorant delivery on most trials (Figure 7A and B), with a minimal detected odorant delivery duration (see Materials and methods) of 72.6 ± 64.3 ms (Figure 7C), though this likely differs for varying operating parameters. Slightly longer valve opening durations (≥50 ms) yielded more reliable odorant delivery (Figure 7D), and all valve opening durations

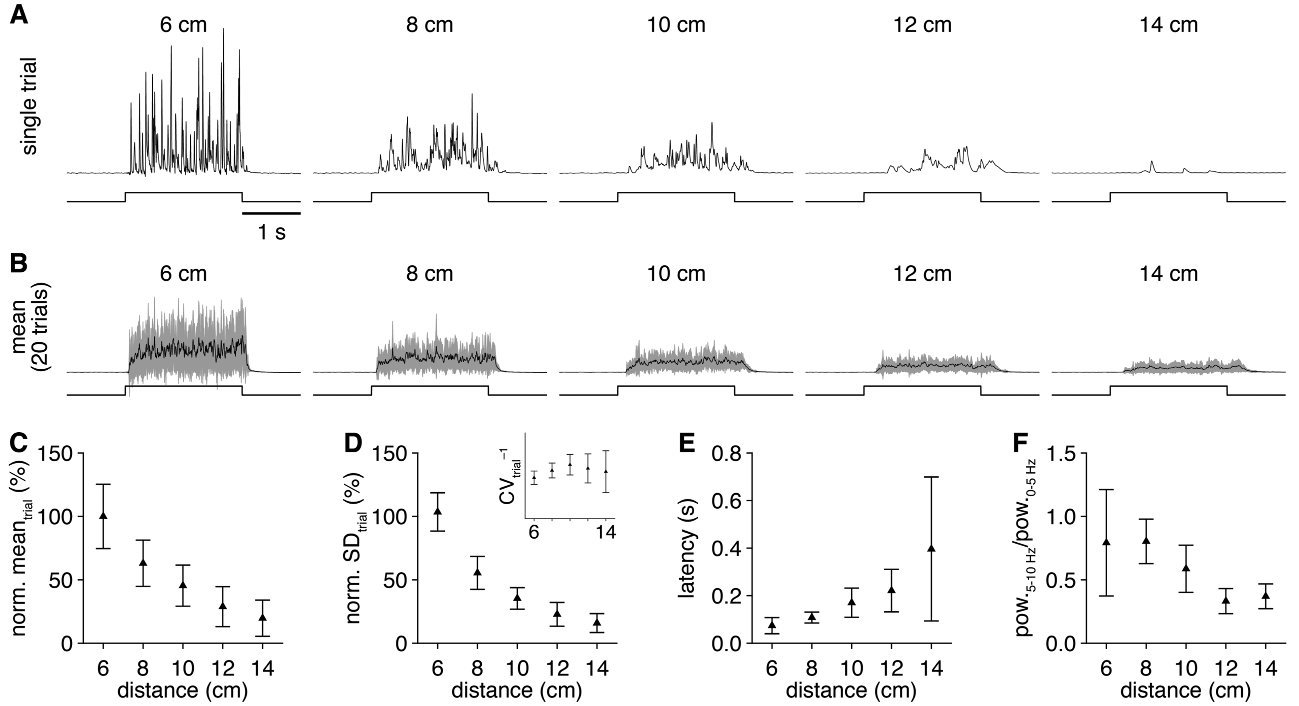

Figure 4 Varying the olfactometer-to-experimental preparation distance modulates the concentration of delivered odorant. (**A**) PID recordings (upper) during single trials of 2-s-long valve openings (lower) from a single olfactometer channel with varying olfactometer-to-PID distances. (**B**) Mean PID recording across 20 trials for each distance tested. (**C** and **D**) PID recording mean (**C**) and SD (**D**) during the odorant delivery for increasing distance (normalized to the 6-cm-distance mean). Inset: inverse of the coefficient of variation for each distance. (**E**) Mean latency of odorant delivery for increasing distance. (**F**) Mean ratio of high frequency (5–10 Hz) to low frequency (0–5 Hz) spectral components in the PID recordings for increasing distance.

≥100 ms delivered odorant at essentially identical rates (Figure 7E) and latencies (Figure 7F), reflecting the steplike mean odorant delivery profile. The novel olfactometer is thus capable of temporally precise odorant delivery across a wide range of stimulus durations.

The novel olfactometer intentionally uses small odorant reservoirs for their disposability, enabling numerous odorants to be delivered without requiring careful maintenance of more permanent reservoirs (e.g., reservoir cleaning, capping loaded reservoirs with an inert gas to limit oxidation). As a consequence of the necessarily small volumes of odorants used, however, odorant volatility may affect the stability of odorant delivery across time. Specifically, odorant delivery across several trials (or prolonged odorant delivery across fewer trials) may substantially deplete the small volume of high volatility odorants. To investigate this possibility, we examined the stability of odorant delivery across 50 consecutive trials of 2-s-long valve openings for 22 chemically diverse odorants (Table 2) ranging from low vapor pressure (Figure 8A and B) to high vapor pressure (Figure 8C and D). As expected, the concentration of odorant delivery decreased across trials, with single exponential decay fits providing odorant-specific time constants of delivery decay (τ_{delivery}) (Figure 8B and D; Table 2). Across the 22 odorants, τ_{delivery} declined in a strongly vapor pressure-dependent manner (Figure 8E) that was well fit ($R^2 = 0.83$) within the vapor pressure (v.p.) range of 0–100 mmHg by Equation (1):

$$\ln\left(\tau_{delivery}\right) = 2.31e^{\left(v.p./717.10\ mmHg\right)} + 3.53e^{\left(-v.p./34.01\ mmHg\right)} \quad (1)$$

Although this delivery decay is thus a limitation of the novel olfactometer design, we note that odorant depletion was slow (i.e., $\tau_{\text{delivery}} > 100$ s) for the majority of odorants tested (Figure 8E; Table 2), thus permitting highly repetitive or prolonged odorant delivery, such as for behavioral training and testing (see In vivo validation: behavior). Further, even high volatility odorants (e.g., 2-butanone) still yielded several seconds worth of relatively stable delivery sufficient for multiple trials of neural recording and/or behavioral testing (though not training across repetitive trials).

In principle, the novel olfactometer can flexibly generate any of 4083 distinct odorant mixtures per 12-odorant panel (i.e., 12 choose 2-12) through the simultaneous actuation of multiple valves, with minimal concern over interchannel contamination given the open airflow design. In practice, however, the dependence of odorant delivery concentration on channel pressure (Figure 5) together with the drop in channel pressure caused by each open valve will limit the total number of simultaneously active channels over which the olfactometer can achieve reliable odorant delivery. To determine this upper limit, we therefore next measured odorant delivery from a single channel while co-activating an increasing number of "blank" channels (i.e., channels with non-photoionizable odorant solvent only loaded into odorant reservoirs), using 40 kPa as a baseline channel pressure. As expected, co-activation of 1 (Figure 9A and B) or 3 (Figure 9C and D) blank channels reduced the mean concentration of odorant delivery (Figure 9G), though still yielded highly reliable odorant delivery with consistent trial-to-trial latencies (Figure 9I). Indeed, reliable odorant delivery could still be detected with co-activation of 7 blank channels (Figure 9E and F), albeit at much lower concentrations (Figure 9G) and slightly more variable latencies (Figure 9I). We thus take 8 as the maximum number of simultaneously active channels that the olfactometer can achieve reliable odorant delivery over (given a 40 kPa baseline channel pressure), supporting the flexible generation of any of 3784 possible odorant mixtures per trial. Depending on the maximal channel

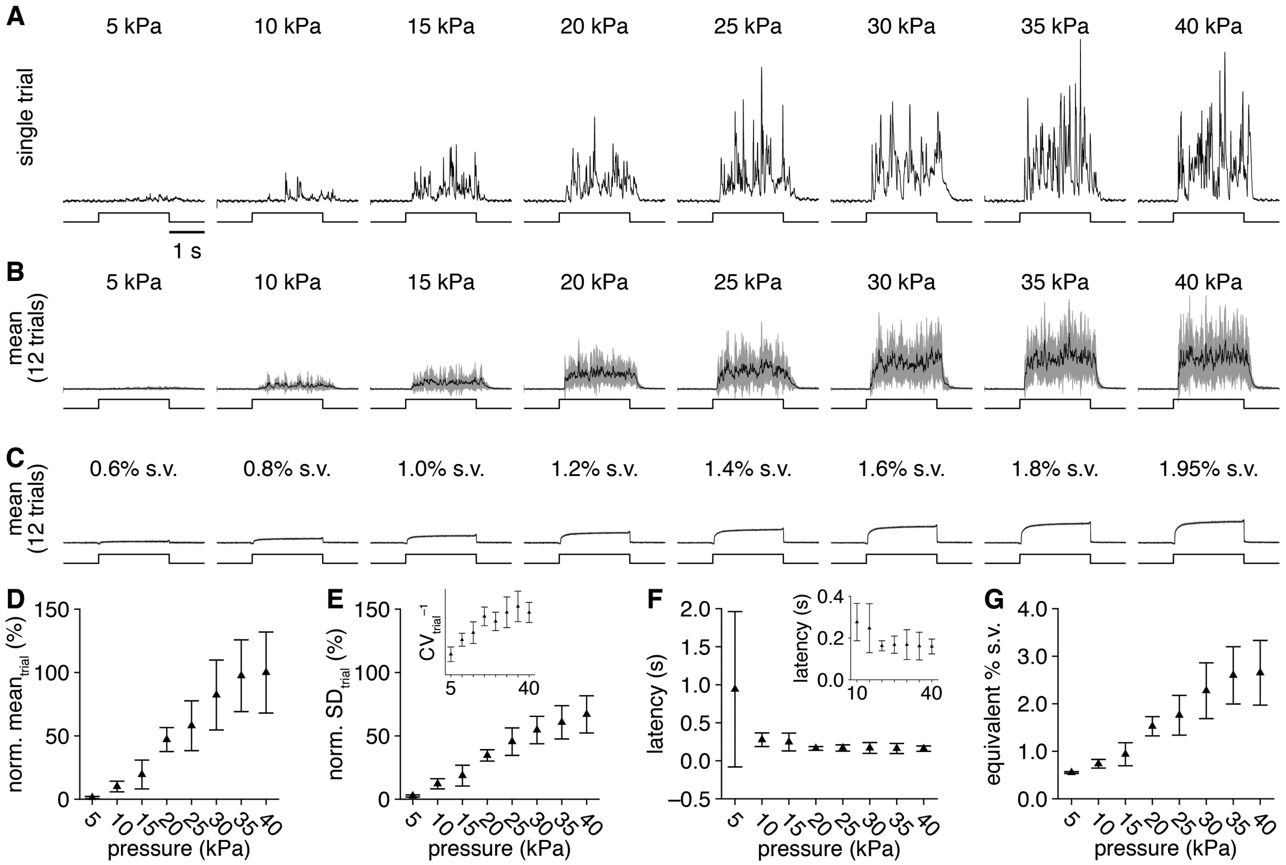

Figure 5 Varying the olfactometer channel pressure modulates the mean concentration of odorant delivery. (**A**) PID recordings (upper) during single trials of 2-s-long valve openings (lower) from a single olfactometer channel with varying channel pressure. (**B**) Mean PID recording across 12 trials for each channel pressure tested. (**C**) For comparison, mean PID recordings (upper) over 12 trials of 2-s-long odorant delivery (lower) of varying-percent saturated vapor from a flow dilution olfactometer. (**D** and **E**) PID recording mean (**D**) and SD (**E**) during the odorant delivery for increasing channel pressure (normalized to the 40 kPa channel pressure mean). Inset: inverse of the coefficient of variation for each channel pressure, demonstrating maximal odorant delivery with minimal variability at 30–40 kPa. (**F**) Mean latency of odorant delivery for increasing channel pressure. Inset: magnification of latencies for pressures ≥10 kPa. (**G**) Relationship between channel pressure and equivalent percent saturated vapor of odorant delivery, calculated from the PID recording mean obtained from the novel olfactometer and a flow dilution olfactometer.

pressure afforded by the clean air source, this limit can also be readily increased to 12 simultaneously active channels and 4083 possible mixtures by increasing the baseline channel pressure to offset the division of airflow across simultaneously open valves.

Standard implementation

On the basis of our PID characterization and our experience from daily use of the novel olfactometer, we recommend the following standard practices and operating parameters for use of the device. Odorants are prepared in advance by diluting each to the desired strength in mineral oil or caprylic/capric medium chain triglycerides—a standard food industry solvent (Zhang and Reineccius, 2017)—to enable flexible selection of 12-odorant panels during an experiment. Odorant panels are then generated immediately before or during an experiment by front-loading each odorant reservoir with 40 μL of odorant using a standard micropipette. This particular volume effectively distributes as a thin layer over nearly the entire internal surface area of the reservoir via gravity and surface tension without leaking from the bottom or impeding airflow (Figure 2C). The use of oil as a solvent facilitates this distribution, whereas water or other hydrophilic solvents do not distribute as evenly across the plastic substrate of the reservoir. Including trace quantities of an odorless dye (e.g., Sudan Black B) in the solvent before odorants are prepared further facilitates the loading process by allowing direct visualization of the distributing odorant within the clear-plastic odorant reservoirs (Figure 2C). When the experimental preparation is ready, we position the delivery arm of the olfactometer 8–10 cm in front of the preparation, enabling both reliable odorant delivery (Figure 4) and easy exchange of the modular barrels without disturbing the preparation. The delivery arm is then locked in place for the duration of the experiment, ensuring equivalent delivery across all odorants tested. A small and quiet air pump with in-line charcoal filter is used to drive carrier stream flow rates of 8 L/min, yielding reliably low-latency odorant delivery (Figure 6) as well as a constant delivery of clean air to the experimental preparation between trials. For initial odorant presentation, channel pressures are typically set to 30 kPa. Any desired change in the concentration of odorant delivered is then achieved by modulating the channel pressure by ±10 kPa (for modest changes) or by preparing an odorant reservoir with a different liquid dilution (for large changes).

In vivo validation: neural imaging

Having systematically characterized odorant delivery from the novel olfactometer using PID recordings, we next tested the ability

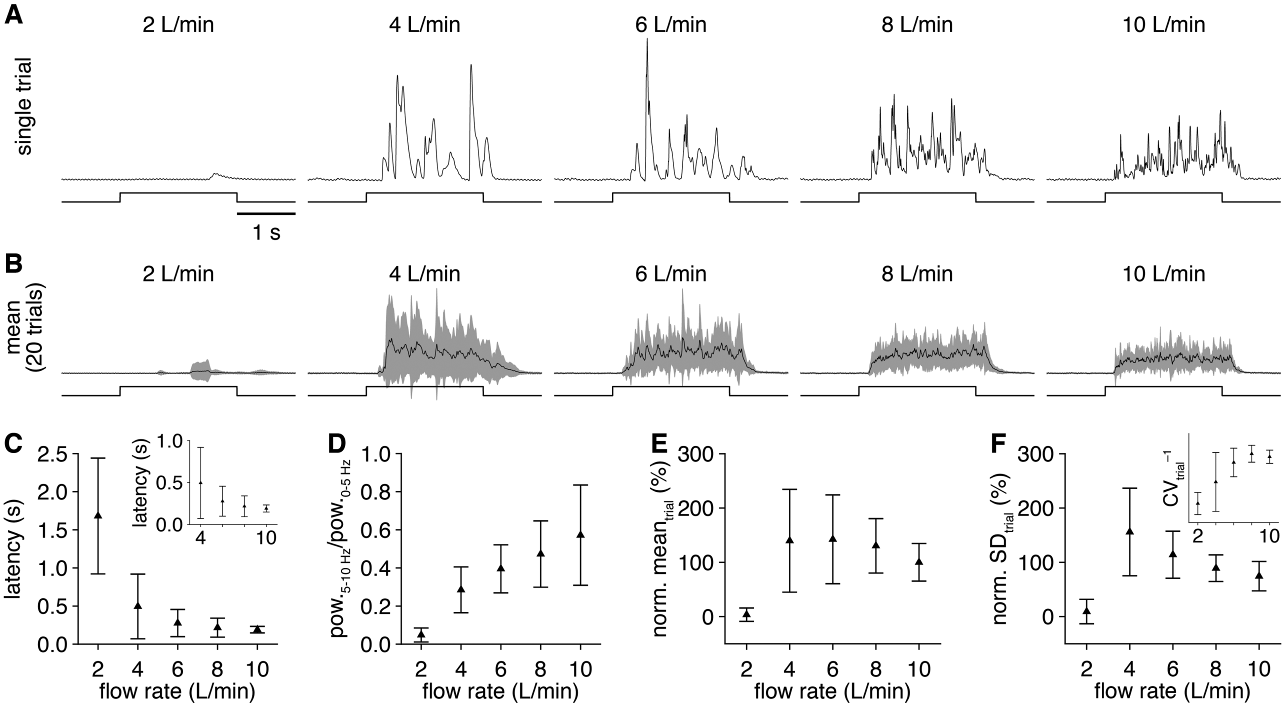

Figure 6 Varying the olfactometer carrier stream flow rate modulates odorant plume dynamics. (**A**) PID recordings (upper) during single trials of 2-s-long valve openings (lower) from a single olfactometer channel with varying carrier stream flow rate. (**B**) Mean PID recording across 20 trials for each flow rate tested. (**C**) Mean latency of odorant delivery for increasing flow rate. Inset: magnification of latencies for flow rates ≥4 L/min. (**D**) Mean ratio of high frequency (5–10 Hz) to low frequency (0–5 Hz) spectral components in the PID recordings for increasing flow rate. (**E** and **F**) PID recording mean (**E**) and SD (**F**) during the odorant delivery for increasing flow rate (normalized to the 10 L/min flow rate mean). Inset: inverse of the coefficient of variation for each flow rate, demonstrating maximal odorant delivery with minimal variability at 8 L/min-flow rate.

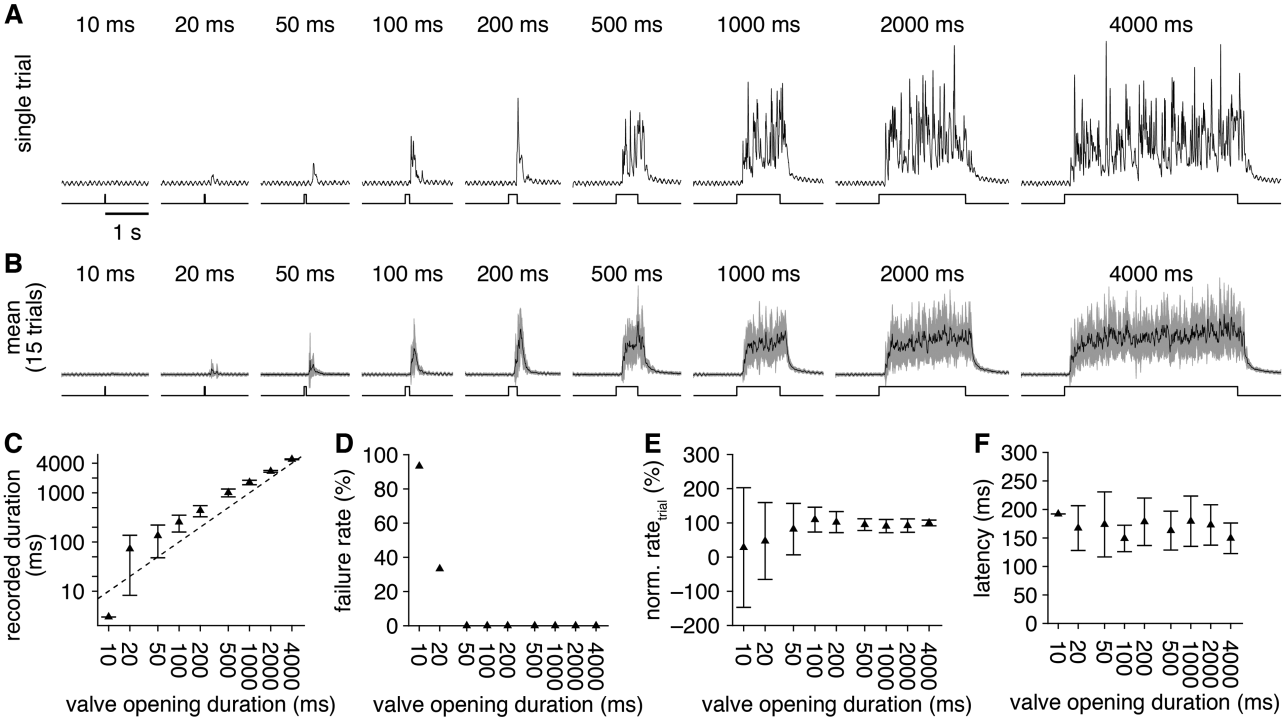

Figure 7 Tightly controlled odorant delivery duration. (**A**) PID recordings (upper) during single trials of odorant delivery with increasing valve opening duration (lower) from a single olfactometer channel. (**B**) Mean PID recording across 15 trials for each valve opening duration tested. (**C**) Mean duration of odorant delivery detected for increasing valve opening duration. Axes plotted on a log-scale. Dashed line: unity. (**D**) Mean odorant delivery failure rate (i.e., percent of trials with no detectable odorant-evoked PID signal) for increasing valve opening duration. (**E**) Mean odorant delivery rate, calculated as the PID recording mean divided by the valve opening duration (normalized to the mean delivery rate with 4000-ms-long valve opening duration). (**F**) Mean latency of odorant delivery for increasing valve opening duration.

Table 2 Vapor pressure-dependence of odorant delivery stability

Odorant[a]	CAS #	Vapor pressure (mmHg, 25 °C)	τ_{delivery} (s)
Acetophenone	98-86-2	0.397[b]	721.09
Benzaldehyde	100-52-7	1.27[b]	191.79
2-Octanone	111-13-7	1.35[b]	551.68
R-(+)-Limonene	5989-27-5	1.98[b]	222.73
4-Methylanisole	104-93-8	2.029[c]	153.18
Heptaldehyde	111-71-7	3.52[b]	398.78
2,6-Dimethylpyrazine	108-50-9	3.873[c]	262.36
(+)-α-Pinene	7785-70-8	4.75[b]	106.20
Isoamyl acetate	123-92-2	5.6[b]	122.00
4-Methyl-3-penten-2-one	141-79-7	8.21[b]	118.77
Hexaldehyde	66-25-1	11.3[b]	103.50
Butyl acetate	123-86-4	11.5[b]	202.83
2-Hexanone	591-78-6	11.6[b]	263.91
Ethyl butyrate	105-54-4	12.8[c]	142.13
2-Methylvaleraldehyde	123-15-9	16.915[c]	66.26
Trans-2-methyl-2-butenal	497-03-0	17.107[c]	117.96
Valeraldehyde	110-62-3	31.792[c]	42.52
2-Pentanone	107-87-9	35.4[b]	34.51
2-Methylbutyraldehyde	96-17-3	49.317[c]	23.58
Isovaleraldehyde	590-86-3	50[b]	28.05
Butane-2,3-dione	431-03-8	56.8[b]	26.77
2-Butanone	78-93-3	90.6[b]	17.43

[a] Prepared at 1:10 liquid dilution.

[b] PubChem (https://pubchem.ncbi.nlm.nih.gov/).

[c] The Good Scents Company Information System (http://www.thegoodscentscompany.com/).

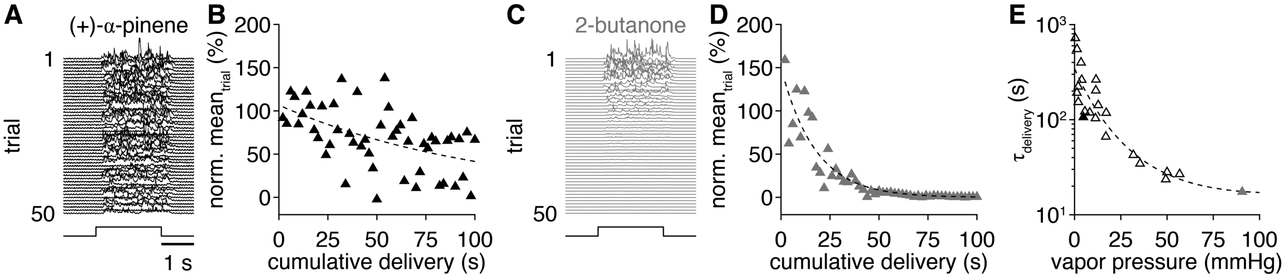

Figure 8 Odorant volatility influences the stability of odorant delivery. (**A**) PID recordings (upper) across 50 consecutive trials of 2-s-long delivery (lower) of a low volatility odorant: (+)-α-pinene (1:10 liquid dilution). (**B**) PID recording mean during the odorant delivery across 50 consecutive trials (100 cumulative seconds) from **A**. Dashed line: single exponential decay fit. (**C** and **D**) Same as **A** and **B** for a high volatility odorant: 2-butanone (1:10 liquid dilution). (**E**) Odorant delivery decay time constants (i.e., τ_{delivery}; from single exponential fits, as in **B** and **D**) for 22 odorants with varying volatility. Solid black and gray points correspond to odorants shown in **A** and **B** and **C** and **D**, respectively. Dashed line: Equation (1) fit.

of the olfactometer to drive reliable odorant- and concentration-specific neural activity. Specifically, we compared spatiotemporal patterns of olfactory sensory neuron activation evoked by 3 chemically distinct odorants presented at 2 liquid dilutions using either a flow dilution olfactometer or the novel olfactometer. Consistent with our previous results in anesthetized mice (Wachowiak and Cohen, 2001; Spors et al., 2006), odorant delivery from the flow dilution olfactometer evoked focal glomerular patterns of odorant- and concentration-specific activity in the dorsal main olfactory bulb, with activity temporally modulated to varying degrees by inhalation (Figure 10A–L). In turn, turbulent delivery of the same odorants at estimated equivalent mean concentrations from the novel olfactometer evoked essentially identical spatiotemporal activity patterns, with only slight differences in activity likely arising from: 1) imperfectly matched final concentrations, 2) distinct odorant delivery latencies, and/or 3) the slower rise to a final steady-state concentration with the flow dilution olfactometer. Our results thus indicate that, within the temporal resolution afforded by our imaging approach, odorant delivery from the novel olfactometer evokes reliable odorant- and concentration-specific neural activity comparable to that observed with a flow dilution olfactometer. Moreover, in contrast to flow dilution olfactometers, which can require long intervals for odorant concentrations to equilibrate within tubing and final delivery ports before effective delivery, the novel olfactometer can deliver distinct odorants at arbitrarily short intervals, as demonstrated by the rapid-fire presentation of 4 odorants within 10 s (Figure 10M and N).

We next turned to a more extensive test of the trial-to-trial reliability and specificity of neural activity evoked by odorant delivery from the novel olfactometer. Capitalizing on the ability of the olfactometer to efficiently deliver numerous odorants, we imaged odorant-evoked activity of olfactory sensory neuron terminals in 105 glomeruli across 73 odorants (including both odorant solvent and empty reservoir negative controls) delivered in a pseudo-random

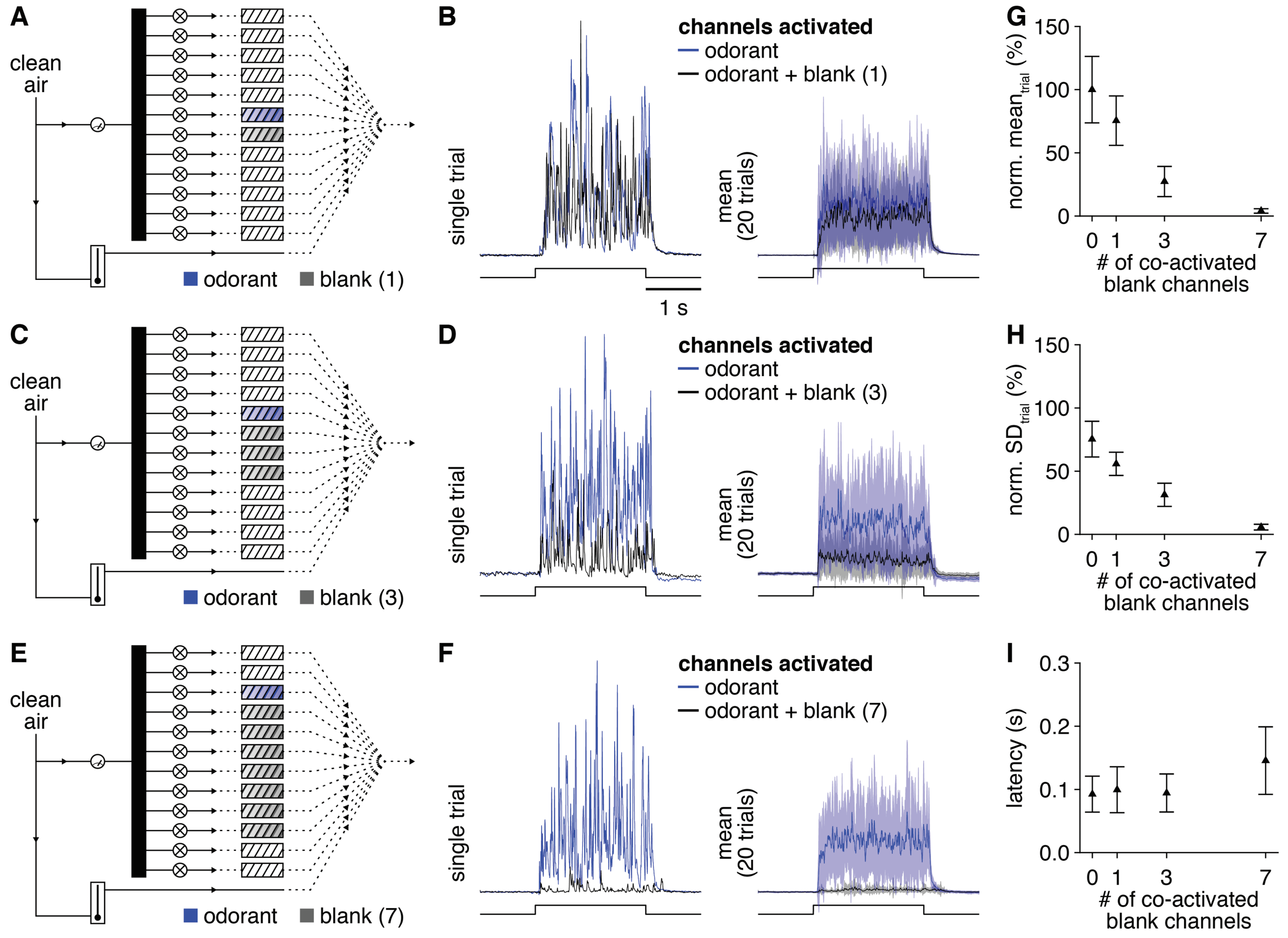

Figure 9 Simple mixture generation with up to 8 individual components. (**A**) Schematic of olfactometer preparation for testing odorant delivery from a single channel in isolation or simultaneously with activation of 1 blank channel (i.e., a channel with non-photoionizable odorant solvent only loaded into the odorant reservoir). (**B**) Single trial PID recording (left) or mean PID recording (right) during 2-s-long valve openings (lower) of the odorant in isolation or the odorant and blank channel simultaneously. (**C–F**) Same as **A** and **B** for 3 and 7 co-activated blank channels. (**G** and **H**) PID recording mean (**G**) and SD (**H**) during the odorant delivery for increasing numbers of co-activated blank channels (normalized to the 0 co-activated blank channels mean). (**I**) Mean latency of odorant delivery for increasing numbers of co-activated blank channels.

order over 219 trials in a single experimental preparation spanning ~75 min from the start of imaging (Figure 11A). Across individual trials, odorants reliably evoked distinct glomerular patterns of activity, including activity in just a single glomerulus when particular odorants were presented at low concentration (Figure 11B). In contrast, within the span of 219 trials, neither the odorant solvent nor the empty reservoir control evoked any detectable neural activity (Figure 11C), confirming a lack of contamination. Finally, correlating responses of all 105 glomeruli across each trial revealed consistently high correlations for repeat trials of the same odorant, whereas distinct odorants evoked glomerular patterns of activity with variable levels of correlation (Figure 11D), as expected from the diverse bank of odorants tested. The novel olfactometer is thus capable of highly efficient and flexible odorant delivery with minimal interchannel and intertrial contamination.

In vivo validation: behavior

In our final set of experiments, we investigated the behavioral performance of awake head-fixed mice performing a go/no-go odorant discrimination task using the novel olfactometer. We began by assessing whether mice could discriminate 2 odorants closely matched in volatility and $\tau_{delivery}$ (estimated using Equation (1)) but highly distinct chemically and perceptually: 2-acetylthiazole (CS+; vapor pressure: 0.173 mmHg; $\tau_{delivery}$: 337.9 s) and *m*-cresol (CS–; vapor pressure: 0.110 mmHg; $\tau_{delivery}$: 340.0 s) (1:10 liquid dilutions). Across 3 days, mice reached 80% accuracy within the first 100 trials and 90% accuracy within the first 260 trials, on average (Figure 12A). While rapid, we note that this rate of learning is slower than some previous studies using standard flow dilution olfactometers (e.g., Bodyak and Slotnick, 1999; Chu et al., 2016), a difference that may reflect our choice of odorants and/or the potentially greater task difficulty imposed by the turbulent odorant delivery.

Following this simple behavioral task, we next evaluated whether the novel olfactometer could be used to administer progressively more difficult tasks by training mice to discriminate binary mixtures of the same 2 odorants mixed in liquid-phase at varying ratios. Indeed, mice learned to discriminate stimuli ranging from 90% 2-acetylthiazole/10% *m*-cresol versus 10% 2-acetylthiazole/90% *m*-cresol to 55% 2-acetylthiazole/45% *m*-cresol versus 45% 2-acetylthiazole/55% *m*-cresol within 1–2 days, with final performance levels well above chance (Figure 12B). Collectively, these results thus demonstrate that the novel olfactometer is well suited for both neural recording and behavioral experiments.

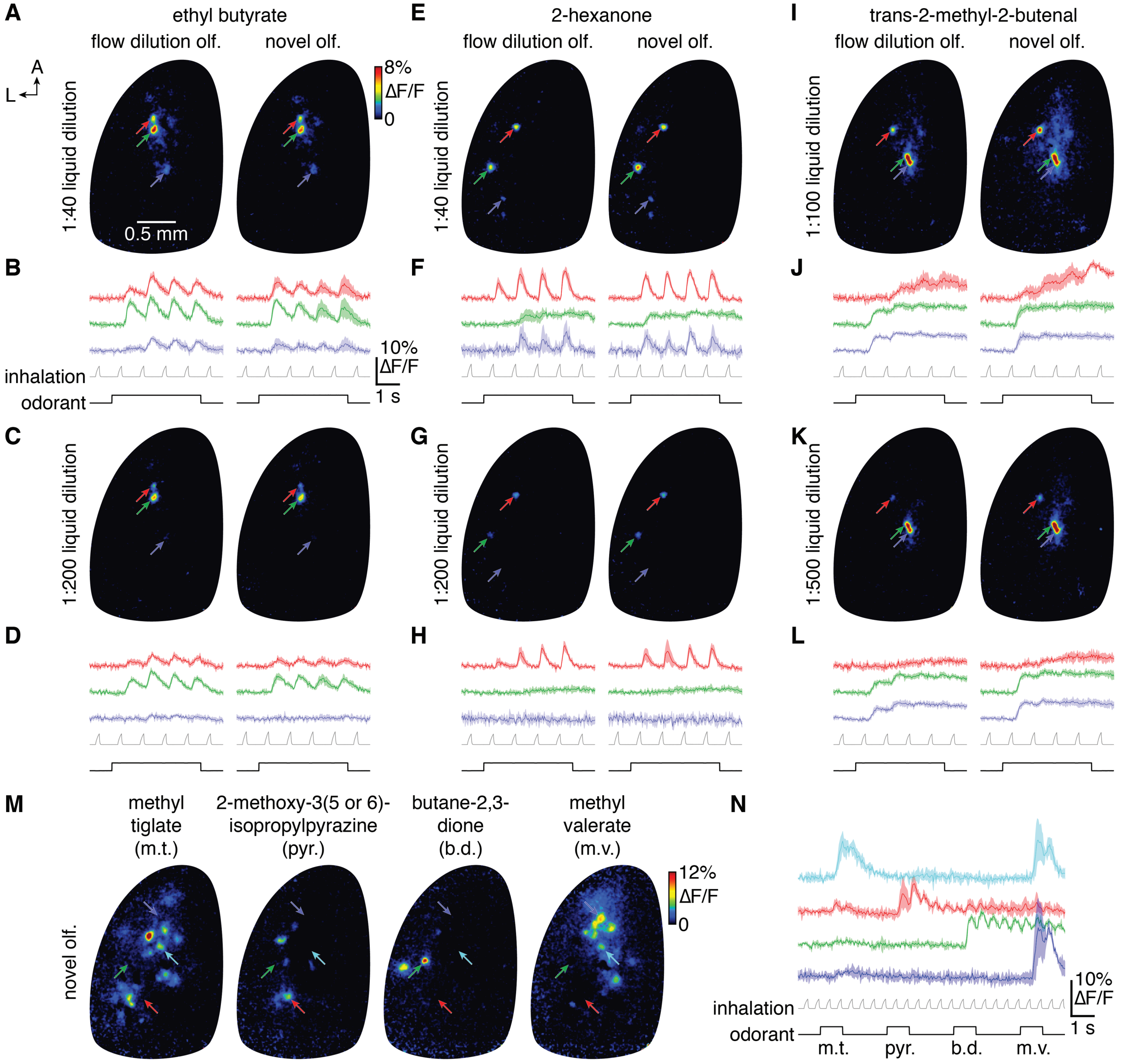

Figure 10 Comparable odorant- and concentration-specific neural activity in the mouse main olfactory bulb evoked by the novel olfactometer and a flow dilution olfactometer. (**A**) Mean ΔF/F map (4 trials) of GCaMP6f responses from olfactory sensory neurons projecting to the dorsal main olfactory bulb of an OMP-Cre;RCL-GCaMP6f mouse following 4-s-long presentation of ethyl butyrate (1:40 liquid dilution) by either a standard flow dilution olfactometer (left) or the novel olfactometer (right). (**B**) Mean activity timecourses of the glomerular ROIs labeled in **A** (upper) relative to pressure measurements of artificial inhalation (middle) and the timecourse of odorant presentation (lower). (**C** and **D**) Same as **A** and **B** for a lower odorant concentration. (**E–L**) Same as **A–D** for the odorants 2-hexanone (**E–H**) and trans-2-methyl-2-butenal (**I–L**). (**M**) Mean ΔF/F maps (3 trials) following rapid sequential presentation of methyl tiglate, 2-methoxy-3(5 or 6)-isopropylpyrazine, butane-2,3-dione, and methyl valerate. (**N**) Mean activity timecourses of the glomerular ROIs labeled in **M** (upper) relative to pressure measurements of artificial inhalation (middle) and the timecourse of sequential odorant presentation (lower).

Alternative designs

The modular and relatively simple design of the novel olfactometer permits a high degree of flexibility in final configuration, depending on the desired performance characteristics. Indeed, not only can numerous operating parameters be easily modulated (e.g., olfactometer-to-experimental preparation distance, channel pressure, carrier stream flow rate, and/or valve opening duration) but multiple components of the olfactometer can also be readily replaced with other commercially available alternatives. For example, mixers for 2-part adhesives (i.e., odorant reservoirs) exist in a wide variety of lengths (e.g., 2.9–5.3 in.), permitting different volumes of odorant to be loaded to achieve different degrees of odorant delivery stability. These mixers likewise are available in a variety of tip styles (e.g., blunt, Luer slip, Luer lock) that are compatible with different odorant reservoir tips (e.g., dental applicators vs. variable-gauge bent needles), effecting different final bore diameters and consequent odorant delivery rates.

Beyond replacing individual components, the novel olfactometer design can also be easily added to, as demonstrated by the addition of an inexpensive mixing eductor (Table 1) to the the carrier stream

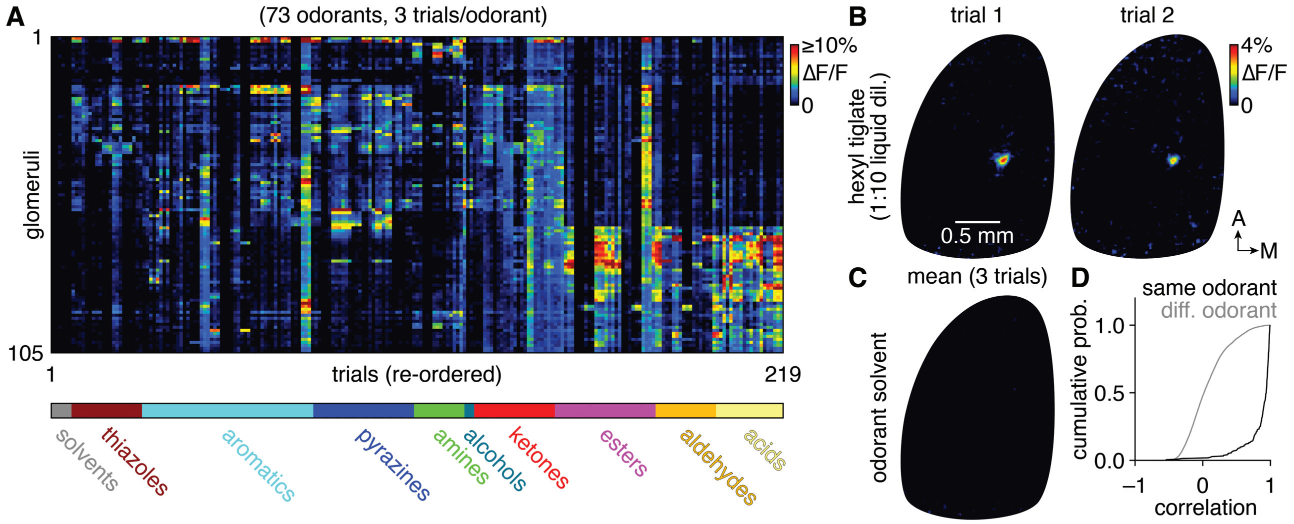

Figure 11 Reliable and efficient odorant delivery. (**A**) Mean ΔF/F GCaMP6f signals from 105 glomeruli in the left main olfactory bulb of an OMP-Cre;RCL-GCaMP6f mouse evoked by 2-s-long delivery of 73 odorants (3 trials/odorant shown; trials reordered so that repeat trials of the same odorant appear sequentially). (**B**) Map of ΔF/F signals in the main olfactory bulb summarized in **A** evoked by hexyl tiglate (1:10 liquid dilution). Two nonconsecutive trials are shown, with 16 trials delivering 11 other odorants interspersed between the 2 trials. (**C**) Map of ΔF/F signals as in **B**, evoked by the caprylic/capric medium chain triglycerides odorant solvent. Mean of 3 trials shown, collected after delivering 12 chemically diverse odorants, demonstrating no detectable contamination. (**D**) Cumulative probability of intertrial correlations of glomerular responses shown in **A**, demonstrating consistently high correlations for the same odorants and broadly distributed correlations for different odorants.

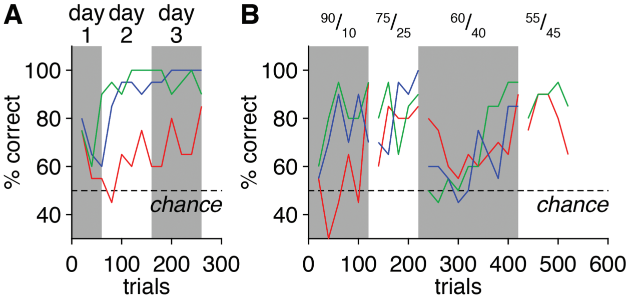

Figure 12 Operant conditioning using the novel olfactometer. (**A**) Behavioral performance of head-fixed mice (*n* = 3) in a simple go/no-go olfactory task requiring discrimination of pure odorants for a water reward. (**B**) Behavioral performance of the same mice in progressively more difficult discrimination tasks requiring discrimination of progressively more similar odorant mixtures.

tube (Figure 13A) to enhance mixing of the odorant within the carrier stream and reduce variance in the instantaneous concentration of odorant delivery. Briefly, an eductor combines an upstream nozzle and downstream conical diffuser separated by a short open span. As fluid (vapor or liquid) passes through the constricting nozzle its velocity increases, generating a decrease in pressure (i.e., the Venturi effect) that draws in surrounding fluid through the open span. The central stream and drawn-in fluid then enter the diffuser at high velocity, whereupon the broadening walls generate turbulent mixing, ultimately outputting a well-mixed stream.

To implement this modification, we attach the eductor to the carrier stream tube and aim the odorant reservoir tips toward the open span of the eductor, allowing expelled saturated odorant vapor (plus surrounding air) to be drawn into the diffuser (Figure 13B) and thoroughly mixed with the carrier stream (Figure 13C). PID measurements of odorant delivery (Figure 13D and E) revealed that addition of the eductor reduced the variance in the instantaneous concentration of odorant delivery (i.e., PID signal SD) by ~76%, which equated to a ~32% reduction in the PID signal coefficient of variation during the odorant pulse (Figure 13G) when accounting for the ~66% increase in mean odorant dilution (Figure 13F). Addition of the eductor also dramatically reduced the variability in latency from valve opening to odorant delivery by ~82% (Figure 13D).

Three caveats must be considered with the optional addition of an eductor. First, the struts connecting the eductor nozzle and diffuser can physically occlude odorant delivery from a subset of the 12 total olfactometer channels, necessitating greater care in positioning of odorant reservoir tips. Second, odorant passing through the eductor is mixed with air drawn in from the surrounding environment, increasing the potential for nonspecific odorant input to the experimental preparation. Exhaust systems positioned around the experimental station can mitigate this effect, however. Finally, the eductor introduces an adsorptive surface to the novel olfactometer that necessarily increases the probability of intertrial contamination. We note, however, that spans of open airflow are still maintained both upstream and downstream of odorant reservoirs independent of eductor addition. Moreover, the relatively laminar flow within the upstream portion of the eductor preserves a boundary layer between incoming saturated odorant vapor and the eductor body, minimizing odorant adsorption. Finally, the modular design of the olfactometer allows for an eductor to be quickly removed and replaced with one of multiple clean eductors at hand during the course of an experiment, further minimizing concerns of intertrial contamination.

Discussion

We have presented a novel olfactometer design and validated its performance using PID recordings, neural imaging, and behavioral testing. The distinguishing novel features of the olfactometer are its mixing of saturated odorant vapor with a carrier stream in free space, and the isolation of odorant reservoirs from the delivery flow path by spans of open airflow. These features greatly reduce the available

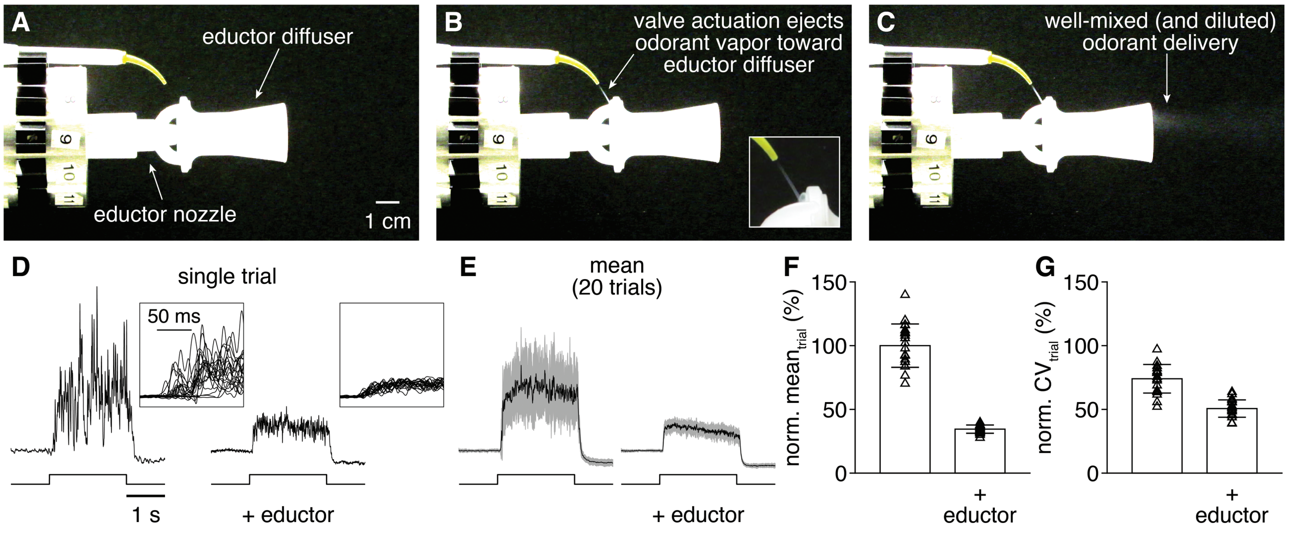

Figure 13 Optional addition of an eductor can reduce odorant delivery variability. (**A–C**) Images of $TiCl_4$ delivery from the novel olfactometer with eductor immediately before valve actuation (**A**), immediately following valve actuation (**B**; inset: magnification of expelled saturated odorant vapor being drawn into eductor diffuser), and following mixing of the expelled $TiCl_4$ with the carrier stream (**C**). (**D**) PID recordings (upper) during single trials of 2-s-long valve openings (lower) from a single olfactometer channel without or with eductor addition. Inset: magnification of odorant delivery onset across 20 trials, demonstrating the reduction in variability of odorant delivery latency with eductor addition. (**E**) Mean PID recording across 20 trials without or with eductor addition. (**F** and **G**) PID recording mean (**F**) and coefficient of variation (**G**) during odorant delivery without or with eductor addition (normalized to the no-eductor mean).

surfaces to which odorants can adsorb as well as the possibility of odorant backflow into upstream manifolds, which collectively minimize both intertrial and interchannel contamination of one odorant with another. Although resulting in turbulent odorant delivery, this design strategy nevertheless permits easy experimental control over the mean concentration, onset latency, and duration of odorant delivery, and further yields delivery that is not only indistinguishable across 12 independent channels but also reliable across trials. Indeed, the trial-to-trial reliability and consistency of odorant delivery enabled different odorants and concentrations to be mapped to neural activity with a level of precision comparable to that obtained with a flow dilution olfactometer, and further supported operant conditioning of mice in an odorant discrimination task. Finally, from a practical standpoint, the novel olfactometer is easily assembled from mostly commercially available components, is relatively inexpensive to construct and use, and its simple design allows for a range of modifications to adapt the device to particular experimental applications.

In addition to detailing our design, a principal goal of this report was to provide potential users with an idea of whether and how well the turbulent delivery afforded by the novel olfactometer may function in their own experimental application and/or setup. Toward this end, we have performed vaporized $TiCl_4$ visualization, an array of PID measurements, neural imaging, and behavioral training. While extensive, further evaluation may still be necessary to effectively implement the olfactometer in new experimental applications and/or setups. In those cases, we hope that the battery of tests performed here may also serve as a general guideline for such evaluations. In particular, we have found that initial $TiCl_4$ visualization followed by systematic PID measurements of olfactometer performance at each new experimental setup to be highly useful, as different setups often have distinct gross patterns of airflow that may influence the turbulent odorant delivery.

Advantages of the novel olfactometer

A primary motivation for developing this novel design was the need to efficiently and flexibly test odorants in the context of mapping sensory information to neural activity in the olfactory system. Addressing this problem requires testing responses to large numbers of odorants—often at multiple concentrations—due to 1) the high dimensionality of olfactory stimulus space, 2) the limited knowledge of odorant receptor tuning, and 3) the limited knowledge of (and animal-to-animal variability in) glomerular positions. Several previous studies have approached this problem by constructing flow dilution olfactometers capable of delivering relatively large numbers of odorants (64–100 per experiment) (e.g., see Davison and Katz, 2007; Soucy et al., 2009; Tan et al., 2010) and their results have provided important insights into olfactory processing. However, with each of these olfactometers, the control of odorant delivery with dedicated lines requires odorant panels to be pre-selected. The requirement to replace these lines and, in some cases, control valves when introducing a new odorant or a new concentration range creates an energy barrier to expanding or modifying a chosen odorant panel. In addition, the use of a common final delivery line, as well as a common upstream supply line, introduces substantial possibility for intertrial and interchannel contamination. In our experience with simpler versions of such flow dilution olfactometers, we have found these issues to pose serious bottlenecks to comprehensively testing large odorant panels, with issues such as intertrial and interchannel contamination becoming increasingly apparent with recent improvements in the sensitivity of tools for monitoring odorant-evoked neural activity.

The novel features of the olfactometer presented here largely solve the issues described earlier. These features, together with the modular design and integration of disposable odorant reservoirs, enable rapid exchange of 12-odorant panels during experimentation, supporting highly efficient and flexible odorant testing. With such a design, odorants and concentrations can be chosen even during the course of an experiment, and the number of total stimuli that can be tested is limited only by the endurance of the experimental preparation and experimenter.

Several additional advantages also emerged as a result of the novel design. First, because each olfactometer channel is essentially independent, delivering mixtures of nearly any combination of 12 odorants in vapor-phase is trivial. Although such mixture generation is somewhat limited in the current implementation by the division of airflow over simultaneously open valves, resulting in a drop in channel pressure (and thus mean concentration of odorant delivery) with increasing mixture complexity, this issue could easily be resolved by using a separately regulated pressure source for each channel. Second, unlike flow dilution olfactometers, there is no time required for washout of odorant from a common final delivery line or for an odorant to reach steady-state concentration within a mixing chamber. As a result, there is practically no limitation to the timing of odorant delivery from different channels: different odorants can be delivered at arbitrarily short intervals relative to one another, and can even overlap in time. This temporal flexibility dramatically increases the efficiency with which odorants can be tested and may further prove useful in examining temporal relationships in olfactory processing. Finally, the novel olfactometer may be of particular utility for investigating the neural encoding and behavioral perception of naturalistically fluctuating odorant stimuli. Such an application is especially well suited for nonmammalian model organisms in which rapidly fluctuating odorant stimuli profoundly shape neural activity, such as locusts (see, e.g., Geffen et al., 2009; Aldworth and Stopfer, 2015; Huston et al., 2015), moths (see, e.g., Vickers et al., 2001), and flies (see, e.g., Nagel and Wilson, 2011; Nagel et al., 2015).

Limitations of the novel olfactometer

Consistent with any olfactometer operating with liquid odorant dilutions, final absolute odorant concentrations delivered from our novel olfactometer are difficult to accurately predict due to nonideal behavior of odorants at the liquid-to-vapor transition (Slotnick and Restrepo, 2005). This difficulty is exacerbated in the novel olfactometer design by the distance-dependent influence of olfactometer positioning on odorant delivery (Figure 4) and the longer-than-typical olfactometer-to-experimental preparation distances (Figure 1E), as well as by the incomplete mixing of expelled saturated odorant vapor with the carrier stream (Figure 6). Thus, the novel olfactometer is not ideal for absolute measurements of concentration–response functions in terms of odorant molarity. Nevertheless, the novel olfactometer can effectively deliver distinct relative concentrations, both through easily prepared liquid dilutions that are loaded into the disposable odorant reservoirs and through instantaneous changes in channel pressure (Figure 5). We have found this level of control to easily support rapid testing of odorants across a wide concentration range, including exceedingly low concentrations capable of revealing highly selective activation of olfactory sensory neurons projecting to single glomeruli. Moreover, with careful positioning of the olfactometer to achieve comparable olfactometer-to-experimental preparation distances (and holding all other flow parameters constant), we routinely observe concentration-specific patterns of neural activity that are indistinguishable across experimental preparations and setups. More quantitative comparisons and analyses may, however, require some initial calibration of the olfactometer using a PID, as performed herein.

The carrier stream flow rates driving reliable odorant delivery from the novel olfactometer (4–10 L/min) exceed the flow rates typical of flow dilution olfactometers (~0.5 L/min). However, even at our standard implementation flow rate of 8 L/min, the broad diameter of the carrier stream tube (~$^1/_2$ in.) renders theoretical maximal airspeeds of only ~1 m/s (~2.4 mph) at the carrier stream tube outlet, and even lower speeds 8–10 cm away, where the experimental preparation is positioned (Figure 1E). Indeed, anemometer measurements confirmed that airspeeds 8–10 cm away from the carrier stream tube outlet are 0.4–0.5 m/s (0.9–1.1 mph) given an 8 L/min flow rate (see Materials and methods; data not shown), speeds well in line with both 1) relatively low natural wind speeds, and 2) the theoretical maximal airspeed (0.4 m/s) delivered by a flow dilution olfactometer with 5-mm-diameter delivery port and 0.5 L/min carrier stream flow rate. These measurements suggest an overall negligible risk of desiccating and/or irritating the experimental preparation nasal epithelium. Consistent with this conclusion, we routinely image neural activity in anesthetized mice artificially sniffing at 3 Hz under a constant 8 L/min carrier stream flow rate continuously for 4–8 h and have observed no time-dependent changes in odorant-evoked neural activity (data not shown). From a more practical standpoint, however, the high carrier stream flow rates of the novel olfactometer may impose some limitations on clean air sources, exhibiting relatively quick depletion of standard gas cylinders. A small air pump with in-line charcoal filter provides an effective and economical solution to this issue.

The novel olfactometer can effectively deliver odorants across a large range of volatility (Figure 8; Table 2). However, due to the open nature of the odorant reservoirs, with no immediately upstream or downstream tubing, extremely volatile odorants (e.g., *N*,*N*-dimethylethylamine, vapor pressure: 495.357 mmHg) can escape the odorant reservoir and enter the carrier stream even when the corresponding channel valve is not actuated (data not shown). The novel olfactometer is thus not suitable for testing such extremely volatile odorants without further modification. Although we have not systematically examined over what range of volatility the novel olfactometer can achieve tightly controlled odorant delivery, in practice we have had excellent success monitoring neural activity in the mouse olfactory system time-locked to channel valve actuation with the vast majority of odorants tested.

Olfactory information is encoded in precise spatiotemporal patterns of neural activity within both vertebrate and invertebrate olfactory systems (Laurent et al., 2001; Schaefer and Margrie, 2007; Chong and Rinberg, 2018). Turbulent odorant delivery from the novel olfactometer may complicate the investigation of such dynamic neural activity by introducing additional temporal variance. Placement of a PID close to the experimental preparation to simultaneously monitor odorant delivery and neural activity could help account for this added complexity. Moreover, variance in the instantaneous concentration of odorant delivery can be substantially reduced by the addition of an eductor to achieve more thorough mixing of the expelled saturated odorant vapor with the carrier stream (Figure 13). At the same time, inhalation (in mammalian preparations) may mitigate this potential confound by low-pass filtering turbulent stimuli. Indeed, using ultrasensitive GCaMP6f to monitor olfactory sensory neuron activity, we observed no difference in the variability of neural activity evoked by turbulent odorant delivery from the novel olfactometer compared with that evoked by comparatively stable odorant delivery from a standard flow dilution olfactometer (Figure 10). Whether comparable patterns of neural activity are maintained using measures of activity with greater temporal resolution than GCaMP6f (e.g., electrophysiological recordings) and in awake, behaving mice warrants further investigation.

Funding

This work was supported by the National Institute of Mental Health [F32MH115448 to S.D.B.], the National Institute on Deafness and Other Communication Disorders [F32DC015389 to T.P.E., R01DC006441 to M.W.], and the National Science Foundation [1555919 to M.W.].

Acknowledgements

We thank Jackson Ball, Gustavo A. Vásquez-Opazo, Thomas Rust, and Rebecca L. Kummer for excellent technical assistance; Neil J. Vickers for generous loan of the anemometer; and Daniel W. Wesson, Andrew K. Moran, Shaina M. Short, and Isaac A. Youngstrom for helpful discussion.

Conflict of interest

The authors declare no competing financial interests.

References

Aldworth ZN, Stopfer MA. 2015. Trade-off between information format and capacity in the olfactory system. *J Neurosci*. 35:1521–1529.

Bodyak N, Slotnick B. 1999. Performance of mice in an automated olfactometer: odor detection, discrimination and odor memory. *Chem Senses*. 24:637–645.

Chong E, Rinberg D. 2018. Behavioral readout of spatio-temporal codes in olfaction. *Curr Opin Neurobiol*. 52:18–24.

Chu MW, Li WL, Komiyama T. 2016. Balancing the robustness and efficiency of odor representations during learning. *Neuron*. 92:174–186.

Davison IG, Katz LC. 2007. Sparse and selective odor coding by mitral/tufted neurons in the main olfactory bulb. *J Neurosci*. 27:2091–2101.

Eiting TP, Wachowiak M. 2018. Artificial inhalation protocol in adult mice. *Bio Protoc*. 8:e3024.

Geffen MN, Broome BM, Laurent G, Meister M. 2009. Neural encoding of rapidly fluctuating odors. *Neuron*. 61:570–586.

Huston SJ, Stopfer M, Cassenaer S, Aldworth ZN, Laurent G. 2015. Neural encoding of odors during active sampling and in turbulent plumes. *Neuron*. 88:403–418.

Johnson BN, Sobel N. 2007. Methods for building an olfactometer with known concentration outcomes. *J Neurosci Methods*. 160:231–245.

Laurent G, Stopfer M, Friedrich RW, Rabinovich MI, Volkovskii A, Abarbanel HD. 2001. Odor encoding as an active, dynamical process: experiments, computation, and theory. *Annu Rev Neurosci*. 24:263–297.

Li J, Ishii T, Feinstein P, Mombaerts P. 2004. Odorant receptor gene choice is reset by nuclear transfer from mouse olfactory sensory neurons. *Nature*. 428:393–399.

Madisen L, Garner AR, Shimaoka D, Chuong AS, Klapoetke NC, Li L, van der Bourg A, Niino Y, Egolf L, Monetti C, et al. 2015. Transgenic mice for intersectional targeting of neural sensors and effectors with high specificity and performance. *Neuron*. 85:942–958.

Nagel KI, Wilson RI. 2011. Biophysical mechanisms underlying olfactory receptor neuron dynamics. *Nat Neurosci*. 14:208–216.

Nagel KI, Hong EJ, Wilson RI. 2015. Synaptic and circuit mechanisms promoting broadband transmission of olfactory stimulus dynamics. *Nat Neurosci*. 18:56–65.

Schaefer AT, Margrie TW. 2007. Spatiotemporal representations in the olfactory system. *Trends Neurosci*. 30:92–100.

Schmidt R, Cain WS. 2010. Making scents: dynamic olfactometry for threshold measurement. *Chem Senses*. 35:109–120.

Slotnick B, Restrepo D. 2005. Olfactometry with mice. *Curr Protoc Neurosci*. 33:8.20.1–8.20.24.

Soucy ER, Albeanu DF, Fantana AL, Murthy VN, Meister M. 2009. Precision and diversity in an odor map on the olfactory bulb. *Nat Neurosci*. 12:210–220.

Spors H, Wachowiak M, Cohen LB, Friedrich RW. 2006. Temporal dynamics and latency patterns of receptor neuron input to the olfactory bulb. *J Neurosci*. 26:1247–1259.

Takahashi YK, Kurosaki M, Hirono S, Mori K. 2004. Topographic representation of odorant molecular features in the rat olfactory bulb. *J Neurophysiol*. 92:2413–2427.

Tan J, Savigner A, Ma M, Luo M. 2010. Odor information processing by the olfactory bulb analyzed in gene-targeted mice. *Neuron*. 65:912–926.

Verhagen JV, Wesson DW, Netoff TI, White JA, Wachowiak M. 2007. Sniffing controls an adaptive filter of sensory input to the olfactory bulb. *Nat Neurosci*. 10:631–639.

Vickers NJ, Christensen TA, Baker TC, Hildebrand JG. 2001. Odour-plume dynamics influence the brain's olfactory code. *Nature*. 410:466–470.

Wachowiak M, Cohen LB. 2001. Representation of odorants by receptor neuron input to the mouse olfactory bulb. *Neuron*. 32:723–735.

Wachowiak M, Economo MN, Díaz-Quesada M, Brunert D, Wesson DW, White JA, Rothermel M. 2013. Optical dissection of odor information processing in vivo using GCaMPs expressed in specified cell types of the olfactory bulb. *J Neurosci*. 33:5285–5300.

Zhang, J, Reineccius GA. 2017. Minimizing flavor deterioration. *Perfum Flavor*. 42:32–49.